Stony Brook University

Observation of Ferroelastic Toughening in Ceramic Oxides by Polarized Raman Spectroscopy

A Thesis Presented

by

Amanda Brooke Schubert

to

The Graduate School

in Partial Fulfillment of the

Requirements

for the Degree of

Master of Science

in

Materials Science and Engineering

Stony Brook University

May 2015

Stony Brook University

The Graduate School

Amanda Brooke Schubert

We, the thesis committee for the above candidate for the

Master of Science degree, hereby recommend

acceptance of this thesis.

Molly Gentleman – Thesis Advisor
Assistant Professor, Department of Materials Science and Engineering

Perena Gouma
Professor, Department of Materials Science and Engineering

T.A. Venkatesh
Associate Professor, Department of Materials Science and Engineering

This thesis is accepted by the Graduate School

Charles Taber
Dean of the Graduate School

Abstract of the Thesis

Observation of Ferroelastic Toughening in Ceramic Oxides by Polarized Raman Spectroscopy

by

Amanda Brooke Schubert

Master of Science

in

Materials Science and Engineering

Stony Brook University

2015

The lifetime and efficiency of turbine engines for applications such as aerospace and power generation rely on the use of thermal barrier coatings (TBC). The TBC provides a thermal barrier between the metallic turbine engine components and the high temperature gas produced by the turbines combustion. They prevent oxidation as well as thermo-mechanical damage of the underlying metallic components. 7-8 weight-% yttria stabilized zirconia (7-8YSZ) is the industry standard material for thermal barrier coatings due to its high melting temperature, high toughness, low thermal conductivity, and high coefficient of thermal expansion which similar to that of the underlying metallic engine components. Although 7-8YSZ has proven to be the best choice for TBC's, erosion damage caused by particles ingested into the engine and the potential for phase decomposition after long-term high temperature exposure has the potential to cause damage and eventual failure of even these coatings. Engineering new tougher materials to replace 7-8 YSZ can address both of these issues.

There are two main mechanisms that are capable of increasing the toughness in zirconia-based ceramics, ferroelasticity and phase transformation toughening. Ferroelasticity is a phenomenon that allows the material to change its orientation through the process of twinning resulting in a shear strain when a mechanical load is applied. Unlike ferroelastic toughing, transformation toughening requires a volume change that is accompanied with the transformation from a metastable phase to a stable phase in the zirconia system. Stabilizer poor compositions of stabilized zirconia exhibit a stable tetragonal phase a high temperature and stable monoclinic phase at low temperature. When cooled, the stabilizer poor composition crosses over a transformation temperature (t_0) that causes a martensitic transformation from tetragonal phase to monoclinic phase. This phase transformation, accompanied with volume expansion, can cause cracking in a porous material - but in dense materials this expansion can lead to compressive stresses that toughen the material.

In general, x-ray diffraction and TEM have been the primary method for studying the phase decomposition and toughening mechanisms in thermal barrier materials and systems. In this study, Raman Spectroscopy has been used explored as a method for exploring the ferroelastic toughening mechanism in both bulk and coated thermal barrier materials. Additionally it was explored as a method for exploring phase stability of these systems.

Dedicated to my parents, my husband, and my children.

Thank you for all your patience, love, and support.

Table of Contents

List of Figures

List of Tables

Acknowledgments

I first and foremost would like to thank Dr. Molly Gentleman for her outstanding guidance over the course of my undergraduate and graduate studies and research. Her mentorship has helped me as a non-traditional student avoid many academic follies while simultaneously illuminating a path to success. In addition I would like to thank all my previous mentors and professors especially Dr. Nicole Zacharia, Michael Krall, and Sylvia Epitropova for all of their guidance and words of encouragement. I would like to thank Dr. Perena Gouma and Dr. T.A. Venkatesh for serving on my committee. I would also like to thank everyone in our group past and present for working as a team, creating an enjoyable research experience.

CHAPTER I

INTRODUCTION

1.1 Thermal Barrier Coating

Gas turbine engines are widely used in the power generation and aerospace industries in order to increase the firing temperature of these high temperature sections[1] for applications such as electric power generation and aerospace[2]. Over the last several decades turbine engine efficiencies have increased due to design development by incorporating lighter and higher temperature tolerant materials as well as improvements in combustion science[2]. The increased efficiency has been accompanied by an increase in combustion temperatures of up to ~ 1500°C [3]. The internal engine components exposed to this extreme temperature, such as the vanes and blades, have melting temperatures ~ 1300°C - imposing a serious threat to the life of these components[1]. To address this challenge, a thin layer of ceramic oxide with low conductivity and a high melting temperature is applied to the surface of metallic structural components to thermally insulate them from the high temperature combustion. These thermal barrier coatings (TBCs) was first applied and tested on turbine components in 1976 by a group at NASA[1; 4]. To achieve strong adherence between the ceramic layer and the metallic layer of the turbine components, a metallic bond coat is generally used as an intermediary. The ceramic top coat, metallic bondcoat, and the oxide layer the thermally grows on top of the bondcoat make up the thermal barrier coating system (TBC)[2; 5] shown in figure 1 .Each TBC layer requires specific combination of material properties for the system to reach this goal. In most cases, the TBC topcoat is about 200 microns thick[6] and can produce a thermal gradient of up to ~ 300°C from the top of the ceramic coating to surface of the underlying engine components illustrated as a red

line in figure[2]. Continuing efforts are being made to increase this gradient as well as the toughness of the ceramic oxide thereby increasing the efficiency and life of the turbine engine.

1.1.1 TBC layers and Properties

The ceramic topcoat, which is situated at the outermost layer and exposed to high temperature gases provides the majority of the thermal insulation for the underlying engine components. To perform this task well, the material that makes up the topcoat must have low thermal conductivity, high melting temperature, high temperature phase stability, strain compliance, a high coefficient of thermal expansion (CTE) similar to that of the underlying engine components, high toughness, and poor sinterability[7; 8]. While moderately low thermal conductivity and high melting temperatures are defined thermodynamic properties for the ceramic composition in use some of the other properties can be engineered. Several of the properties noted above refer to the thermo mechanical performance of the material. This is because foreign objects are commonly ingested into the engine impacting the turbine engine blades and potentially damaging the brittle ceramic coating[9; 10]. To avoid failure during these types of events, the topcoat must be engineered to avoid severe mechanical failure upon impact at elevated temperature. One engineering solution is the design of materials that ferroelastically switch on impact with a foreign object. These ceramic oxides can undergo toughening by ferroelastic switching when strained[11-13]. Materials can also toughen by phase transformation during high temperature operation to overcome the brittle failure[14-18]. Another way to improve the thermo mechanical performance of the coating is to reduce the sinterability of ceramics resulting in significant amounts of porosity being maintained, in the coating and producing three valuable properties: increased the surface exposure to the high temperature gas to assist in

lowering thermal conduction, increased strain compliance, and reduced centrifugal force by weight reduction decreasing the strain at the ceramic and bond coat interface[2].

Beyond the topcoat, the bondcoat must possess properties that match both the ceramic topcoat and the underlying engine components. The CTE must be similar to the thermally grown oxide and the engine components to minimize stress caused by expansion and contraction during operation cycles[5]. As described earlier, a thermally grown oxide layer (TGO) of alpha-alumina is formed between the bond coat and ceramic oxide layer. In order for the ceramic oxide layer to stay adherent to the underlying components over the expected life of the TBC the TGO must be phase compatible with the ceramic oxide and not grow above a critical thickness that causes the coating to spall[19; 20].

The underlying engine components typically account for 40-50% of the engines weight and are made from lightweight single crystal nickel or cobalt based superalloys with CTEs of ~10 ppmC^{-1} [2]. Figure 2 [2] shows the CTE vs thermal conductivity for several materials. Looking at the shaded areas, ZrO_2 has similar CTE to that of Nickel alloys and has low thermal conductivity making ZrO_2 a good candidate for the ceramic oxide coat.

1.1.2 The Current TBC Materials and Challenges

Pure Zirconia has a monoclinic structure at room temperature and upon heating transforms into tetragonal ~1100°C, then to cubic ~2300°C (merle). The transformation between monoclinic and tetragonal is accompanied by a ~4% volume change. To avoid this phase transformation, the zirconia is doped with another oxide such as Yttria. The current ceramic oxide used in TBC's is 7-8% yttria stabilized zirconia[1] with a high CTE of ~9.5 ppmC^{-1}, similar to that of the nickel based super alloy engine components, and a low thermal conductivity ~

3W/mK[2] 2. The yttria stabilizes the zirconia tetragonal crystal structure at temperatures above 1050°C by diffusing into oxygen vacancies created when zirconia is doped with yttria[21].

Looking at the phase diagram of yttria stabilized zirconia (YSZ) in Figure 3[2], the dashed box region is 7-8% YSZ, a metastable tetragonal phase (t') created by rapidly cooling the phase from the cubic phase field, does not cross over the tetragonal to monoclinic transformation line (T_{t-m}) during heating and cooling. However, upon long term exposure to high temperature, the t' phase will decompose into a two phase, Y-rich (cubic) and Y-poor (tetragonal) compositions of YZS[21; 22]. The Y-poor composition, when heated and cooled, crosses over the T_{t-m} line creating the 4% volume change illustrated in figure 4. This volume change is accompanied by cracking and eventually failure of the coating. Extensive research to stabilize zirconia with different size cations and/or introducing different amounts of oxygen vacancies, to avoid phase decomposition during long exposure to high temperatures, is vital for a prime reliant TBC.

NiCrAlY is the most commonly used bond coat composition with a contiguous CTE transition between the oxide coat and the nickel base superalloy components[23-25]. This allows for cycling of the turbine engine with the absence of stress building at the interfaces, as the turbine components expand and contract[2]. The bond coat also protects the underlying superalloy from oxidizing by producing a TGO layer between the bond coat and ceramic topcoat [4; 5]. Once the TGO reaches a critical thickness, the ceramic oxide as well as the underlying components will have an increased rate of degradation[23; 24]. The NiCrAlY bond coat forms Al_2O_3, the slowest growing oxide, at high temperatures[2] - making this an optimal choice for TBC applications.

There are two common processes used to apply the ceramic topcoat to the engine components, air plasma sprayed (APS) and electron beam physical vapor deposition (EB-PVD). The microstructures developed by these processes play an important role for the overall function

of the TBC, Figure 5. During the APS process the oxide powder is fed into an arc plasma sprayer where the high temperature, high velocity gas stream instantly melts the powder and accelerates it to the surface to which it is being applied. This process causes a puddled/splat microstructure with a high surface roughness and large pores parallel to the substrate surface[3; 26]. The EB-PVD process, conversely, takes place under vacuum. A billet of oxide-based ceramic is vaporized by an electron beam that then solidifies onto the surfaces of the engine components resulting in a columnar microstructure with a relatively smooth surface[4; 9; 27; 28]. The EB-PVD process is usually reserved for rotating and high load engine components where the higher strain compliance and fine surface roughness achieved by the columnar structure are required. These coatings also have lower erosion rates than the microstructure produced in APS coatings providing more durable and longer lasting coatings for the underlying substrates[29; 30].

Although extensive research has been done on the material, application, and fabrication for all layers of the TBC, a prime reliant TBC system that can withstand high temperatures and maximize the turbine engines efficiency, has not yet been achieved. The current TBC system can protect the underlying turbine components at high temperature but over time the ceramic topcoat suffers from phase decomposition and severe erosion by particles ingested into the turbine engine. Both of these threats on the TBC can be addressed with implementation of a new high temperature stable, high toughness ceramics.

1.2 Toughening of TBC's

Multiple mechanisms can produce toughening in ceramic materials. These processes can be divided into two categories; through the control the size of flaws in the components or by using toughening mechanisms that result in the component becoming insensitive to the size of

the flaws present[31]. Due to the environment that thermal barrier coatings are exposed to during their regular operating conditions including the continual bombardment by high speed sand particles and other foreign objects, structural dependent toughening mechanisms are required for the survival of these coatings. In zirconia based systems two main structural toughening mechanisms have been identified to date: transformation toughening and ferroelastic toughening. While phase transformation toughening is restricted to low temperatures because of its dependence on a metastable phase a low temperature transformation, ferroelastic toughening is assumed to be able to take place at any temperature where the ferroelastic phase is present.

1.2.1 Transformation Toughening

The toughness of zirconia-based ceramics, which are the basis for current state of the art TBCs, ranges widely from $\Gamma ss \approx 6\ Jm^{-2}$ for cubic zirconia[12; 32] which is untoughened to $\Gamma ss \approx 210\ Jm^{-2}$ for partially stabilized zirconia[15] that exhibits transformation toughening and highly toughened[33-36]. Transformation toughening occurs when a material under stress transforms from one phase to another. In the case of partially stabilized zirconia or zirconia compositions where the tetragonal phase can pass through the tetragonal to monoclinic t_0 line on cooling, transformation toughening is accomplished through a series of processing steps. First the partially stabilized composition in pressed into a green body of the desired shape. It is then sintered at a temperature that produces the high temperature tetragonal phase throughout the material. When the material is cooled, sintering constrains the material preventing the transformation to the monoclinic phase that requires a volume expansion. This phase is then only triggered when the ceramic is damaged. A crack can provide the activation energy for the

phase transformation, but the associated volume expansion will immediately reclose the crack toughening the ceramic.

Transformation toughening can only take place below transformation temperature. Although transformation toughening is well understood and very effective, it is limited to temperatures below (~600-900°C[13; 31]) where the required phase transformation is allowed. TBCs however, operate in the range of ~1000-1500°C. As a result, this mechanism is ineffective for toughening thermal barrier coatings and other high temperature materials during their operation.

1.2.2 Ferroelastic Toughening

There are some compositions of stabilized zirconia that have been identified that have higher than expected toughness without undergoing transformation toughening[37; 38]. This increase in toughness is as a result of ferroelasticity in those compositions[13]. Ferroelasticity is a temperature independent process that is defined by a material having at least two energy equivalent states that the material can move between as the result of an applied load. The movement between states creates and energy hysteresis loop that can result the absorption of energy upon a single switching event increasing the toughness of the material.

In Ferroelastic materials, the force required to initiate the ferroelastic process is called the coercive stress coercive stress, σ^T. The increase in toughness associated with the ferroelastic process, $\Delta\Gamma$, follows the following relationship:

$$\Delta\Gamma = 2f\sigma^T \varepsilon^T h \qquad (1)$$

where f is the volume fraction of the material that undergoes ferroelastic switching in the process zone, h is the width of the process zone, and ε^T is the ferroelastic strain that is 2/3(c/a - 1), where c/a is the tetragonality of the bulk material. In metastable tetragonal t' phase the

ferroelastic process takes place by the formation of 90° {110} type twin boundaries. Because of the tetragonality in the crystal the formation of these twin domains results in permanent shear strain in the material out of the direction of loading. This ability of the material to absorb energy through the reorientation of the crystal during ferroelastic process is what gives them superior toughness.

CHAPTER II

PREVIOUS STUDIES

2.1 Toughness by Tetragonality

The increased toughness that results from the ferroelastic process comes from stresses around a crack reaching the stress required for activating the ferroelastic process. This results in a permanent shear strain in the material through the formation of twin boundary domains[12]. The mechanism for the increased toughness is therefore the energy absorbed by the reorientation of the tetragonal domains that are present around the crack to the new orientation[13]. The stress required for domain switching is called the coercive stress, σ^T, and is related to the increase in toughness as described by Equation (1) as described in section 1.2.2[31].

In this equation, ε^T is described as the ferroelastic strain induced by the domain reorientation and is defined by $\varepsilon^T = 2/3(c/a - 1)$ where c/a is the tetragonality for a tetragonal ceramic (Equation 2). From this equation and equation (1) it can be seen that three parameters control the increase in toughness that comes from ferroelastic toughening: the tetragonality (c/a), the coercive stress, and the process zone size. The tetragonality is the easiest to measure and modify and has therefore been most studied. Several new high toughness ceramic coating materials have been proposed with some success[39; 40]. The Ti-Y co-doped zirconia composition fabricated in reference [40] showed great toughness in bulk materials, but failed to be successful in coating tests[41] and when tested in here these materials showed evidence of transformation toughening, not ferroelastic toughening, by Raman spectroscopy. The Ta co-doped materials on the other hand had high tetragonality, but lower than expected toughness[39].

2.2 Gentleman Ferroelastivity Results

The first step in determining the usefulness of Raman spectroscopy at measuring the effectiveness of ferroelastic toughening was to determine if ferroelastic switching could be observed in a ceramic when damage was induce. This was completed in the work of Bolon and Gentleman[44] on ceria-stabilized zirconia. In this study bulk ceramics of 18 mole-% ceria stabilized zirconia were indented with a vickers indenter and the surfaces of the indented ceramics were mapped by polarized confocal Raman spectroscopy. Small samples of these ceramics were then loaded in a diamond anvil cell modified to provide uniaxial loading was then used to monitor the crystal orientation under loading. The process zone size and coercive stress were measured from these ceramics.

Process zone measurements. After indenting the surface with a diamond Vicker's indenter, a map of the intensity ratios was made of the surface by moving the Raman collection over the surface. This map along with a white light image of the indent is seen in Figure 6. The white light image shows no contrast between grains or around the cracks, but the Raman map reveals contrast due to crystal orientation. In areas away from the indent, grains on the order of 10 μm are clearly seen in the Raman map. The grains appear constant color showing that they each contain a single orientation domain like those seen in TEM studies[12]. Further inspection reveals that the cracks starting from the tips of the indent appear white as they pass through otherwise dark grains. This white region is the ferroelastic process zone. Measurements of the width of this process zone around several cracks emanating from the indent resulted in an average width of the process zone being approximately 1μm. It was also possible to observe whole grains that had ferroelastically twinned following loading.

Coercive Stress measurements. Coercive stress was also measured for 18-mole percent ceria stabilized zirconia. This was done by placing a small cube of material inside of a diamond anvil cell with the gasket removed so the sample was loaded unaxially. A grain with a large c-axis out of plane intensity was identified and the orientation of that grain was measured as a function of load. The load at which the orientation of the grain began to change was identified as the coercive stress ~300 MPa as seen in Figure 7. Raman maps of the grain during loading also showed the formation and motion of the ferroelastic domain with load.

2.3 Raman Spectroscopy

Raman Spectroscopy, first discovered in 1928 by Sir Chandrasekhra Venkata Raman, is an inelastic light scattering technique that examines the bonding structure of materials by probing the material with a coherent light source. In materials science, it is a nondestructive method used to study electronically polarizable solid matter for information about the bonding structure, defect structure, stress state, and composition of the material[42]. A Raman spectrometer consists of a monochromatic light source, optical microscope, and optics to guide the light source through the system to analyze samples. When the light interacts with the material, vibrational modes of the material change the incident photons wave frequencies through interactions with phonon modes, the change in these frequencies can be used to study the materials state, phase compositions, and crystal orientation.

2.3.1 Science of Raman Spectroscopy

When a monochromatic light, produced by a laser with frequency in the visible, ultraviolet, or near infrared, impinges on a material, the photons scatter both elastically and

inelastically. The majority of the photons scatter elastically and the material and the photons have an equal but opposite change in energy. Conversely, approximately $1x10^{-6}$ of the incident photons interact with the material inelastically. During these interactions, the vibrational modes of the material interact with the photon. The strength and energy of the interaction is dependent on the polarizability of the material, which is founded in the structures inter- and intra-atomic forces[42]. These vibrations will cause an energy transfer, gain or loss, between the photon and the material. The direction of the energy transfer is dependent on the materials starting and ending vibrational states--ground or excited. The, Planck-Einstein relation summarizes the change in energy due to scattering

$$\Delta E=h(\Delta v);\ E_f-E_0,\ \Delta v=v_f-v_0 \quad (3)$$

where ΔE is the change in energy of the photon, E_0 is the initial energy of the photon, E_f is the energy of the photon after interaction with the material, h is Planck's constant, Δv is the change in frequency of the photon, v_0 is the initial frequency of the photon, and v_f is the frequency of the photon after interaction with the material. When the photon scatters inelastically off of a material energy can either absorb energy from or transfer energy to the material in the process thereby changing the energy of the photon: increased frequency and decreased frequency respectively. When the energy of the photon is increased it is known as anti-Stokes scattering, when it is decreased, it is known as Stokes scattering. A schematic of this phenomenon can be seen in figure 8. Because, anti-Stoke scattering requires a thermal population of excited states, the probability of observing this form of Raman scattering is significantly lower than for Stokes scattering for solids at room temperature. As a result, in this study all Raman scattering studies were of Stokes shift lines.

2.3.2 The Raman System

Several components comprise a Raman spectrometer, each of these components play an important role on its performance. An inline laser is guided by steering mirrors through a series of neutral density filters, pinhole, optical microscope, to the sample and then scattered back through the optical microscope and diverted to a Raman filter, slits, and holographic grating to a charged couple-device (CCD) for signal detection. The path of the laser beam is illustrated in figure 9.

The neutral density filters are used to attenuate the power of the laser beam through absorption and reflection without compromising polarization or collimation of the beam. The reduction of the laser's intensity is necessary in many scenarios for example when the sample being examined has an absorption band similar to that of the laser frequency or when the sample is fragile and high laser power may burn or ablate the surface of the sample. In these cases the sample may experience localized heating due to the laser that can result in damage of the surface that is undesirable for the collection of high quality Raman spectra and hence the power is reduce for data collection. Following the neutral density filters in the beam path, the laser passes through a pinhole. In addition to aiding in alignment of the spectrometer, the pinhole trims the shape of the beam improving the quality of "mapping" image resolution. After the pinhole, mirrors guide the beam to the optical microscope and the sample. Here the beam hits the sample where some of the monochromatic light changes frequencies depending on the vibrational modes in the sample (Raman scattering) and is scattered back up through the optical microscope to the Raman filter. The Raman bandpass filter deflects the elastically scattered light from the sample as well as any anti-Stokes scattered light. Only Stokes scatter light passes to the slits and grating. The mechanical stilts following the Raman filter provide confocality for this system.

The opening of these slits allow for the selection of the volume of light from the sample to be passed to the grating. The grating has thousands of grooves per millimeter that deflect the light wavelengths at different angles, creating a diffraction pattern on the CCD (charge coupled device). These create a diffraction pattern that breaks the scattered light from the microscope up and spreads the signal out onto the CCD to that it can be read out as a spectrum. The higher the lines per millimeter the higher the special resolution of the spectrum collected. Finally, the signal is projected on the Peltier cooled CCD. The CCD creates an electrical signal from the incoming photons that results in a Raman spectrum.

Raman systems can be equipped with a range of laser frequencies to accurately analyze different types of materials. Materials generally have an absorption edge such that,

$$V=E_E h \qquad (4)$$

where V is the wave frequency, E_E is the band gap of the material, and h is Planck's constant. Absorption of the exciting light occurs if the wave frequency satisfies hV>Eg. If this occurs, scattering will be very week Raman analysis difficult. To avoid absorption of the excitation frequency the use of lower frequency lasers is often employed. Likewise, high frequency lasers, such as UV lasers, have advantages as well. Raman measurements using visible lasers cause often be plagued with fluorescence bands making it hard to distinguish between the two. The use of UV lasers can eliminate this problem. It should be noted, however, each laser frequency requires the corresponding neutral density filters, gratings, holographic filters, and pinholes in order to maximize the spectral resolution.

2.3.3 Understanding the Raman Spectrum

A Raman spectrum is the representation of materials polarizable vibrational modes as they interact with the incident laser radiation. It is presented as peaks plotted in an energy verses intensity graph where the x-axis is energy and the y-axis is intensity. The x-axis is given in Raman shift wavenumbers, or energy from the incident laser energy. This means that the zero value is the energy of the laser energy. As for the spectrum, the position, widths, and intensity of the peaks are related to the polarizability of the material. The polarizability of the material depends on the atoms location, size, and bonds present in the material. Therefore every material has its own unique spectrum. Analysis of the spectrum can reveal the crystal structure, orientation, and the stress state of a material. To obtain this information the Raman spectra must be analyzed using peak fitting software applications such as Renishaw WiRE (used here) or other programs like Grams AI. All peaks of real solid materials must be fit using mixed Gaussians and Lorentzian curves. This fit is also known as a full Voigt fit. This is a combined fit of the Gaussian curve for a perfect crystal that would "ring down like a bell" and a vibrational energy dissipation for a gas-like structure based on collisions—Lorentzian. From this fit, the intensity, width, and position of each peak can be calculated. An example of curve-fitting can be seen in Figure 10. The peak position gives the average energy for the given vibrational mode where the width is a measure of the distribution of energies being measured. In this study, widening of the peaks is generally due to disorder in the crystal lattice due to defects, grain boundaries and inclusions. Different crystal structures will have a different arrangement of modes at different energies that is specific for the structure. When a material is under strain, the frequency of the vibrational modes is constrained corresponding to shifts in peak position. Just as the strain cause peaks to shift left or right on the x axis, the intensity of the peaks shift up and down along the y

axis due to strain in the material as well. In a polarized spectrum, the intensity of peaks relative to one another can be used to determine the orientation of crystal. A collection of Raman spectrums taken over the surface can be used to create a map of the structure of the surface. That can then be used to study properties like ferroelasticity specifically its process zone size, the state of the material, and phase compositions over areas such as cracks, impacts and other defects along with their surrounding areas. This will be discussed further and is the basis of this thesis.

CHAPTER III

MATERIALS AND METHODS

3.1 Stabilization Experiments

In order to study transformation toughening and ferroelastic toughening in zirconia based ceramic oxides, 7 atomic-% rare earth oxide stabilized zirconia, as well as, 12% and 15% cerium stabilized zirconia powders were processed using standard powder processing techniques and studied. For either transformation toughening or ferroelastic toughening to take place in these ceramics it is necessary for the high temperature stable tetragonal structure to be present at low temperature for transformation toughening or for at whatever temperature the ferroelastic switching is taking place. To accomplish this either sintering constraints or atomic level distortions are required in the lattice. Specifically, sintering constraints are used to mechanically constrain the tetragonal phase in transformation-toughened materials while point defects are used in the case of ferroelasticity.

Point defects are most commonly achieved in zirconia ceramics by doping the host with different size trivalent and tetravalent cations that stabilize the tetragonal structure. The stabilization process takes place by a rearrangement of the anion lattice. For dopant atoms that introduce oxygen vacancies, (large trivalent ions) the distortion is achieved through the reduction of the oxygen coordination around the Zr4+ ions. In the case of small tetravalent ions, the large and small cations order with alternating coordination where the smallest cations are tetrahedrally coordinated. By studying the role of dopant valency and size allows for studies to determine the effects local lattice distortion on the process zone size and coercive stress due of the ferroelastic process. In this work Raman spectroscopy was utilized to determine the phase compositions and

orientation, as well as, the state of stress of the material to determine if the material underwent ferroelasticity or transformation toughening after a load was applied.

3.1.1 Materials

Trivalent rare earth oxides are the perfect choice for examining the role of cation size and therefore lattice strain on the ferroelastic process. This is because of the systematic contraction in ionic size from lanthanum to ytterbium. For this study erbium (Er), gadolinium (Gd), ytterbium (Yb), neodymium (Nd), and lanthanum (La) trivalent ion dopants and cerium (Ce) tetravalent ion dopant were selected as stabilizers for zirconium oxide. All of these dopants have been shown in the literature to have the ability to form a metastable single tetragonal phase when doped to appropriate compositions into zirconia.

As stated previously, the trivalent dopants stabilize the zirconia monoclinic crystal structure into the tetragonal structure by substituting for the zirconium atom on the zirconia sites. In the case of trivalent atoms, one oxygen vacancy is then produced for every two dopant atoms that substitute onto the lattice. A schematic of this process is seen in figure 11. These oxygen vacancies then go preferentially to the sites associated with the zirconium atoms. This is because the small size of the zirconium atom leads to crowding of the oxygen atoms around it and the presence of oxygen vacancies thus relieves the strain associated with the overcrowding.

The basic features of the yttria-zirconia phase diagram is typical for all rare earth oxides with zirconia. Because the stabilization for with trivalent ions is based on overcrowding of the zirconium site by oxygen atoms, the trivalent cation size can produce average cation coordination numbers ranging from 6 to 8. This results in different variations in lattice distortion with trivalent cation size. Likewise, tetravalent cations stabilize zirconia by producing alternating

tetrahedral and dodecahedral coordination around the cations due to the size difference in the zirconium and cerium cation. These two stabilization regimes can be used to determine the role of size of dopant size, presence of vacancies, atomic spacing, and the effects of stability of the ceramic oxides on the ferroelastic process including coercive stress and the process zone size.

3.1.2 Methods

To develop the ceramic powders needed for these studies, several powder processing techniques were used to engineer powders of specific characteristics and compositions that are relevant to each study. Particle size, composition, and phase of the powders is of the utmost importance for the study of phase stabilization and transformation toughening. Reverse co-precipitation on aqueous salts into an ammonium hydroxide solution produces non-agglomerated powders with uniform distribution of the cations in the powder. The powders made using this technique can be further refined using a ball mill to obtain the correct particle size. Sub-micron particles can be obtained in this way. The particle size is important to the densification of samples during sintering. The powders are then processed further, depending on the studies being performed, by pressing into green bodies, sintering, sectioning, polishing, and indenting.

The powders were fabricated from aqueous solutions made from the following nitrate salts: 99.9% Sigma-Aldrich Yb^{3+}, Er^{3+}, Nd^{3+}, La^{3+} and Gd^{3+} nitrates ($RE(NO_3)_3$) Sigma-Aldrich Zirconium acetate solution ($ZrO(C_2H_3O_2)_2$) and 99.5% Alfa Aesar Cerium nitrate hexahydrate ($Ce(NO_3)_3 \times 6H_2O$). These were mixed in appropriate quantities to form 7 atomic-% RE Stabilized Zirconia and 12 atomic-% and 15 atomic-% Cerium Stabilized Zirconia (CSZ) oxide powders. Following the work of Ciftcioglu and Mayo the powders were produced by reverse co-precipitation through the steps below. Calibration of the nitrate and acetate powders were

completed as follows. 1) The nitrates were individually dissolved in de-ionized water and the zirconium acetate was used as raw form. 2) A small amount of each of the liquid solutions and a small amount of zirconium acetate were dried for 24 hours under a heat lamp to form gels. 3) The gels were then placed in a Thermolyne muffle furnace and heat treating them by a series of steps with a ramp rate 10° per minute: room temperature to 400°C, held for 30 min, 400°C to 900°C, held for 2 hours, then cooled back to room temperature. 4) The moles of oxide per gram of liquid solution were calculated by finding the difference in the initial weight of solution (de-ionized water and nitrate) and the resulting weight of the oxide. This allowed for calculations to find out how many grams of each liquid would be needed for reverse co-precipitation process.

Table 1 shows the quantity of each solution used in order to make 10g of each oxide. The liquid solutions were then mixed and poured into a buret dispenser and reverse co-precipitated into a solution containing 200ml of de-ionized water and 150ml of ammonia hydroxide (NH_4OH) while maintaining pH9+. This produced an endothermic reaction resulting in the formation of precipitates of the gel that would be later calcined into the oxide powder. Following precipitation, the precipitates were vacuum filtered and subsequently dried in a fume hood for two hours using a Buchner funnel and an Erlenmeyer flask connected to a vacuum pump. They were then placed into a crucible and dried for 24 hrs under an infrared heat lamp. After that time had passed, the powders were moved to a muffle furnace and calcined by heating them to 900°C with a ramp rate of 10° per minute, held for 2 hours, then cooled 10° per minute. The powders were then mixed with 20 g of 5mm 1kg YSZ beads, and 30 g of methanol in low density polyethylene cylinder containers in preparation for ball milling. U.S. Stoneware mill was used at 60 rpms, for 24 hours in order to reduce the particles to sub-micron size. The beads were then

filtered out of the slurry, and the slurry was dried under a heat lamp. Raman spectroscopy was completed on each of the powders to verify its crystal structure.

After the completion of powder fabrication, the powders were pressed into green bodies, following Ashutosh[43] using a one half inch hardened steel die and a carver press at 850 MPa. The green bodies were then sintered at 1250℃ for 2 hours in a high temperature muffle furnace (MTI KSL-1700X). Raman spectroscopy was then used to verify the presence of the tetragonal phase of the pellets after sintering. Pellets with tetragonal phase were then polished with Buehler silicon carbide abrasive grinding disks, starting with the most abrasive, 240/ 52.2 µm finish, in series to the least abrasive, 1200/ 15.3 µm finish lastly polishing the samples with Buehler Micro Polish Alumina Powder and Suspension resulting in a polished surface with roughness of ~ .05 µm. The polished samples where then indented using a Buehler micromet hardness tester fixed with a Vickers tip. Indents were made on the sample using 500g of force for 5 seconds to produce indents with cracks radiating out from the indent. The resulting crack lengths were measured using an optical microscope. Raman maps were made of the indents around the areas of the cracks using 514nm laser excitation and a 50x objective. The step sizes of the maps are 0.5 µm in the x and y directions and the laser collections times were 5 seconds using 100% laser power.

3.2 Cranfield EB-PVD Samples

A series of EB-PVD thermal barrier coatings were obtained from Cranfield University, Cranfield, United Kingdom for preliminary characterization by polarized-confocal Raman spectroscopy. These samples were characterized both from the top surface as well as after fracture surfaces were produced at Stony Brook University.

3.2.1 Materials

These coatings were produced by EB-PVD at Cranfield University to be 8YSZ in composition and approximately 150 microns in thickness. They were deposited onto one-inch single crystal sapphire buttons approximately 5 millimeters in thickness. Three surface conditions were prepared and studied: as-deposited, samples eroded at 30^{o} impingement angles of impact, and samples eroded at 90° impingement angles of impact. High temperature, high velocity erosion testing was carried out at Cranfield University in their erosion rig described in reference[29]. The samples were eroded with 100 micron alumina balls at an ambient temperature of 800 $^{\circ}$C and velocity of 200 m/s. Impingement angles of either 30° (shallow) or 90° (normal) from the plane of the surface were used. Figure 12 shows white light images of resulting thickness of the samples after erosion.

3.2.2 Measurements

Following erosion, the samples where characterized using polarized confocal Raman spectroscopy. Raman spectra were recorded on samples using a Renishaw inVia mapping microRaman spectrometer outfitted with a Leica microscope and with 488 and 457 (Ar-ion) nm in-line gas lasers. Wavelength and intensity calibrations were completed using a 520 cm^{-1} Si-band from an internal silicon standard for the 488 and 457 nm laser.

For mapping studies, a pinhole was inserted into the beam path increase the accuracy of the location of the measurement and a slit size of 25 microns was used to obtain high confocality. For surface maps, two four-second integrations were used at 100% laser power. Data were collected at one-micron x and y-steps throughout the area of the map. The z-focus was kept constant. Imaging of the fracture surfaces was completed using the 488 nm laser with one by one

micron steps over the area. Spectra were processed using Wire 4.1 software. Prior to peak fitting, the spectral areas were normalized to an area of 1 and an offset baseline was subtracted from all spectra. Peaks were fit using full Voigt curves. From this fit it was possible to determine the intensities from the integrated areas under the curves as well as peak width and peak position. The peak areas were then used to produce the maps of the relative peak intensities with each pixel mapping the relative area of the B_{1g}/A_{1g} for the spectrum collected for that point on the surface. The Raman maps for these studies were taken off the fracture surfaces, the virtual cross sections, and the surfaces illustrated in figure 13, A, B, and C respectively. In addition to these sets of maps, the as-deposited sample was indented with a Buehler micromet hardness tester fixed with a vickers tip for 5 seconds at 200g. Indents were made on the side of the sample, perpendicular to the coatings columns. Maps were taken of the indent using a 488 nm laser and .5 micron x and y step size.

3.3 Neutron diffraction and Raman spectroscopic comparison with ceria-stabilized zirconia

Experiments were completed by the author, Bolon and Gentleman[45] to determine the accuracy of Raman-based coercive stress measurements. Because coercive stress is generally best measured from the bulk by neutron diffraction studies, coercive stress measurements were made on 18 mole-% ceria-stabilized zirconia under compressive loading by both neutron diffraction and Raman scattering. These studies were used to validate the accuracy of Raman spectroscopy studies as well as address any possible sources of error in both of the techniques.

3.3.1 Materials

The ceramic samples used in this study were composed of 18 mole-% ceria-stabilized zirconia. The samples were fabricated using standard powder processing techniques. Commercially available cerium oxide (99.9% Sigma–Aldrich) and zirconium oxide (99.9% Sigma–Aldrich) powders were milled together in the appropriate composition ratio and in methanol using zirconia beads for 24 h. Following milling the powders were dried, crushed, and cold pressed into green bodies in the form of 25.4 mm square prisms. The samples were then sintered at 1500°C for 48 h. This resulted in bulk polycrystalline samples with greater than 95% density and an average grain size of approximately 10 μm. The samples were cut into approximately 10 mm × 10 mm × 20 mm rectangular prisms and polished so that the ends were parallel and surface defects were minimized. Raman spectra and neutron diffraction patterns were collected to confirm the presence of single tetragonal in the materials.

3.3.2 Experiments

Neutron diffraction studies were carried out on the Spectrometer for Materials Research at Temperature and Stress (SMARTS) time-of-flight diffractometer at the Los Alamos Neutron Science Center (LANSCE). The SMARTS system utilized polychromatic neutrons from a pulsed spallation source (wavelength, λ, typically in the range of 0.5–4°A), with the collimated neutron beam impinging on the sample at 45° to the loading axis. A set of two banks of fixed position He-detector tubes were positioned at right-angles to the incident beam such that banks 1 and 2 detected neutrons with diffraction vectors perpendicular and parallel to the loading axis respectively. The time-of-flight (TOF) of the neutrons, from emission to detection, was used to calculate wavelength *via* De Broglie's equation. Samples were loaded in compression at

temperatures ranging from 20°C to 1200°C by a servo hydraulic load frame and high temperature furnace suite within the SMARTS system as seen in figure 14. Temperature was monitored using both a control thermocouple, located in the hot zone as well as a second thermocouple placed on the surface of the sample. The sample temperature was allowed to equilibrate for 30 min prior to each measurement. Diffraction data were collected for 30 min at each strain–temperature condition. The relative intensities of the individual {004} and {200} peaks from neutron diffraction experiments were determined by peak fitting using GRAMS AI software. The peaks were fit to a Gaussian curve with leading and trailing exponentials and a linear baseline. One thousand iterations were used to allow the peaks to converge with the collected data and the integrated area under the fitted curve was recorded. Raman spectra were recorded on samples prior to and following neutron diffraction studies using a Renishaw inVia mapping microRaman spectrometer outfitted with a Leica microscope and 532 nm in-line laser. For these studies a 1800 line/mm grating was used to maximize spectral resolution (∼1 cm−1). Wavelength and intensity calibrations were completed using an internal silicon standard using the 520 cm−1 Si-band. For mapping studies of the ceramic surface, 1s integration times were used at 100% laser power. Mapping images were assembled by rastering an automated *xyz*-motorized stage in 0.5 μm *x*- and *y*-steps while holding the *z*-focus constant. Spectra were processed using Wire 3.2 software. Prior to peak fit-ting, the spectral areas were normalized to an area of 1 and an offset baseline was subtracted from all spectra. Peaks were fit using Voigt curve and relative peak intensities (integrated area under the curve), peak widths, and peak positions were recorded. In addition to surface characterization of the samples by Raman spectroscopy, sister samples of the dimensions of 2 mm × 2 mm × 1 mm thick where fabricated for uniaxial loading in a diamond anvil cell whose gasket has been removed and has been

outfitted for *in situ* Raman measurements. A ruby standard was included in the cell in series with the ceria–zirconia sample to provide luminescence measurements of the stress applied to the sample. These samples were designed to provide a direct comparison between measurements of coercive stress made by the Raman spectroscopic technique described by Bolon and Gentleman[42] and those made by neutron diffraction. Measurements of coercive stress were made by mapping the surface of the sample using Raman spectroscopy and measuring the change in the integrated intensity of Raman bands corresponding to the *c*-axis aligned with the direction of loading (B_1g) as compared to those out of alignment with the loading direction (A_1g).

CHAPTER IV

RESULTS AND DISCUSSION

4.1 Stabilization

18 mole-% ceria stabilized zirconia was selected for the initial ferroelastic toughening studies because the tetragonal to monoclinic t_0 line is below room temperature at that compositions[44]. To look at the effect of composition of ceria on the ferroelastic toughening parameters 15% and 12% ceria stabilized zirconia were also fabricated using the same methods described in 3.1.2 with the exception of the cold press force and sintering process. These samples were pressed at 185 MPa and heat treated to 1500°C with a hold time of 48 hours and a ramp rate of 20°/min. 60 x 60 micron Raman maps were then taken of the indents using polarized Raman spectroscopy with a 514 nm laser and .5 micron x and y step size.

When indented, 15 mole-% ceria stabilized zirconia exhibited ferroelastic toughening around indents in bulk ceramics shown in figure 15, but the spectra revealed the presence of free CeO_2 present in the ceramic. As a result, no conclusions could be made about the actual composition of the ceramic pellet except that it was less than 15 mole-% ceria stabilized zirconia. Likewise measurements made on 12 mole-% compositions also exhibited the peak for pure ceria in the Raman spectrum. Unlike the 15% composition, this composition had completely transformed to the monoclinic phase suggesting the composition was far enough off from 12% due to the lack of incorporation of ceria that the tetragonal phase all crossed the t_0 line on cooling.

4.2 Canfield EB-PVD Samples

Raman maps taken of these surfaces using 488 nm laser excitation showed limited contrast over the surface, but significant differences were observed between the as received and eroded samples. Table 2 shows an approximately 40% increase in the B_{1g}/A_{1g} ratio for the 90^o eroded sample with respect to the as-deposited sample. The samples in Table 2 were t-tested to confirm that the differences between the three conditions were significant. In all cases p-vales of 0.000 were obtained with confidence levels set at 95%.

Confocal "virtual cross sections" were then collected. To achieve this the microscope was fitted with a super long working distance objective and the focal plane was set to the top surface of the thermal barrier coating. Spectra were then collected at two-micron steps along a line on the surface and then the stage was raised two microns and spectra were collected progressively back along the same line. This process was repeated to depths of at least 50 microns into the coating using the 457 nm laser. The results of these "virtual cross sections" for the top 50 microns of the coatings are seen in Figure 16 along with histograms of the Raman peak ratios calculated for those maps. The as-fabricated coating shows no significant contrast over the thickness of the coating that was measured. This is confirmed in the histogram, which shows a single normal distribution centered at 0.32. The virtual cross sections collected for the 30^o eroded and 90^o eroded coatings both exhibit regions at the surface of the coating (top of the image) where the B_{1g}/A_{1g} ratio is significantly higher than the surrounding material. These appear to be evidence of ferroelastically switched twins at the surfaces of these coatings. These regions are evidenced in the histograms by small populations of materials with B_{1g}/A_{1g} ratios at approximately 0.35 and 0.4 while the rest of the coating had populations centered at 0.23 for the 30^o and 0.28 for the 90^o eroded coatings respectively.

Fracture surfaces were created and Raman maps were taken on all surfaces using 488 nm laser excitation. Spectra were collected at one-micron steps over the area. Images were created using the overall Raman scattered intensity as well as the B_{1g}/A_{1g} ratio maps. Raman scatter intensity maps were used in place of white light imaging because of the high roughness and optical transparency of the thermal barrier coatings. These images provide views of the surfaces where it is possible to locate features including column cracks. B_{1g}/A_{1g} ratio maps provided information about the orientation of the coating fracture surfaces being examined. Parts a, c, and e of Figure 17 are Raman scattering intensity images of the as-deposited, 30^o eroded, and 90^o eroded coating fracture surfaces respectively. The adjacent images (b, d, and f) are the B_{1g}/A_{1g} ratio maps for those same areas.

The images for the as received coating show relatively continuous columns and no contrast or crystallographic orientation as observed in figure 17(b). The eroded samples in contrast exhibit extensive cracking, some of which are denoted by arrows in both sets of images. The orientation ratio maps for the eroded samples also reveal significant contrast and several "hot spots" around cracks that appear much brighter than the surrounding materials. These regions are believed to have ferroelastically switched as a result of the cracking process resulting in twinning and the change in orientation observed by Raman scattering. It is also noted that there are many regions where cracks are present without evidence of ferroelasticity as seen in the examples of the arrows in the upper regions of figures 17d and 17f. The dark region at the bottoms of images, c and e and the corresponding regions in d and f correlate to the sapphire substrate.

To gain further knowledge of how mechanical loading triggers ferroelastivity in the EB-PVD coatings, Raman maps were collected of the indent on the as-deposited sample. Indenting

the single crystal columns perpendicular to c-axis shows to induced ferroelastic switching along entire columns shown in the B1g/A1g map in figure 18(b). The white light image figure 18(a) shows the position of the indent, at the center bottom on the image, and damage to the columns from mechanical loading.

4.3 Neutron and Raman Comparison

Samples in their as fabricated state appeared white and semi-opaque following a post-polishing annealing step in air at 1000°C. Samples that were tested in the SMARTS system at elevated temperature appeared gray to black following loading due to oxygen nonstoichiometry induced by their exposure to high temperatures while under vacuum. The neutron diffraction patterns revealed a single tetragonal phase of the P42/nmc space group for all temperature and load conditions tested. An example of neutron diffraction pattern for a sample at room temperature and nominally zero load is seen in figure 19. During the loading in compression the areas under the {004} and {200} peaks of the neutron diffraction pattern were monitored in the banks parallel and perpendicular to the direction of loading. When plot-ted as a function of the compressive load, this data can then be used to determine the coercive stress by identifying the load at which a preferred orientation begins to appear in the material. These data for tests run at 30°C, 800°C, and 1200°C are seen in figure 20. Curve fitting of these using a population increase logistic function of the form:

$$\frac{1}{(1+exp\,(-a(\sigma-\sigma^{T})))^{C}} + \text{offset} \qquad (5)$$

where *a* and *c* are fitting parameters, revealed that although the rate of population growth increased following onset as the temperature increased, the coercive stress remained constant

over the temperature range tested. For 30°C measurements, coercive stresses of 195±21 and 365±13 MPa were measured in banks 1 and 2 respectively. At 800°C those values were measured to be 164±65 and 248±31. And at 1200°C they were 225±1 and 224±3. The error values here are derived from the curve fit described above. The {004}/{200} ratio for the direction parallel and perpendicular to the direction of loading in the neutron diffraction studies was then compared directly to the measurements made using the diamond anvil *in situ* Raman spectroscopic technique. Raman spectra taken at a range of loads under this uniaxial loading condition are seen in figure 21 and illustrate the relative changes in the intensities of the *B*1g (317 cm−1) and *A*1g (249 cm−1) modes as the sample is loaded. It is shown that at loads at approximately of 250 MPa and above, the intensity of the *B*1g mode begins to decrease while the intensity of the *A*1g mode increases. The results of the neutron and Raman diffraction techniques were then compared for the room temperature tested sample. Figure 22 is a plot of the out of plane peak intensities ({004} for neutron diffraction and *B*1gmode for Raman scattering) divided by the in-plane peak intensities ({200} for neutron diffraction and *A*1g mode for Raman diffraction) for the two techniques. This plot shows that although the samples tested in the diamond anvil cell failed at lower loads than the sample tested at LAN-SCE, both techniques reveal significant nonlinearities in the orientation load curves beginning at ∼195±21 – 365±13 MPa for the neutron scattering and 250±23 for the Raman scattering. The dissimilar slopes after the coercive stress between the Raman and neutron scattering data are related to the growth rates of the populations of volume with each orientation and the relative sensitivities of two techniques and are therefore not relevant in determining the coercive stress. The difference in coercive stress between banks one and two observed for room temperature measurements were surprisingly large and the error values given above were generated as a result of fit-ting the data in figure 22

with Eq. (5). This is likely because of the significant amount of scatter seen in this data resulting from interruptions in the neutron source. Although care was taken to limit variability data points like those circled in figure 22 may be as a result of such interruptions to the experiment. When these two data points are excluded from the curve fit, the dash-dot line curve fit seen in the figure is produced for bank 2, and yields a coercive stress of 250±17 MPa which is in direct agreement with the Raman scattering result.

Observations at the surface of samples loaded at high temperature

After compressive failure, the free surfaces of the samples studied by neutron diffraction were examined using Raman spectroscopy to identify any evidence of preferred ferroelastic domain orientation. Figure 23 displays images of the relative intensities of the *B*1g/*A*1g modes on those surfaces. Regions appearing bright indicate out of plane orientation of the *c*-axis suggesting ferroelastic domain reorientation during loading. It is clear from this figure that loading at elevated temperatures lead to an increase in the volume of out of plane oriented grains observed at the surfaces of the tested materials. This is better quantified in the histograms of the normalized intensities for these images available in figure 24. In this figure it can be seen that the median volume of out of plane domains, as measured by the *B*1g/*A*1g ratio, increases with the application of load at temperature. The 1200°C sample shows a more diffuse distribution likely due to the development of a thin layer of the monoclinic phase on its surface. This phase was not present in the neutron diffraction data confirming that the phase was not present in significant quantities, but none the less, obscured Raman measurements at the surface as Raman scattering is highly sensitive to the presence of the monoclinic phase. As a result, this sample alone was

lightly polished prior to these measurements, possibly changing the measurable volume of the out of plane tetragonal phase at the surface.

CHAPTER V

CONCLUSIONS

The major hypothesis of this work was that Raman spectroscopy was a powerful tool for the characterization of the performance and failure of thermal barrier materials and coatings and that it could potentially surpass techniques like neutron and x-ray scattering for routine evaluation. The reasons for this this hypothesis is because of the ease of use of Raman spectroscopy and its non-destructive nature for ceramic characterization. Additionally, because of the way in which Raman works by looking at polarizabilities of the structure, new information about the defect structure of the ceramic is revealed. This is particularly important in oxide ceramics like thermal barrier materials where the metastable behavior is dictated by the anion defect structure.

The studies in this thesis revealed that polarized confocal Raman spectroscopy can be used to measure the presence of ferroelasticity in bulk ceramics and that this technique is as effective at measuring coercive stress as neutron scattering (Bolon, **Schubert**, et. al.)[45] in bulk ceramics. Additional studies with other compositions were also completed here with mixed results. Following this success it was then shown to be possible to directly observe ferroelastic toughening in eroded thermal barrier coatings using the same technique (**Schubert** et. al. *submitted).*

The overall conclusions of this thesis are 1) Raman spectroscopy is a powerful tool for observing ferroelasticity in thermal barrier materials and coatings, 2) Results obtained by Raman spectroscopy match those produced by neutron scattering for coercive stress, and 3) Studies of

eroded coatings reveal the importance of ferroelasticity in the erosion process illuminating opportunities to increase the toughness of new materials previously unknown.

Appendix

Figures

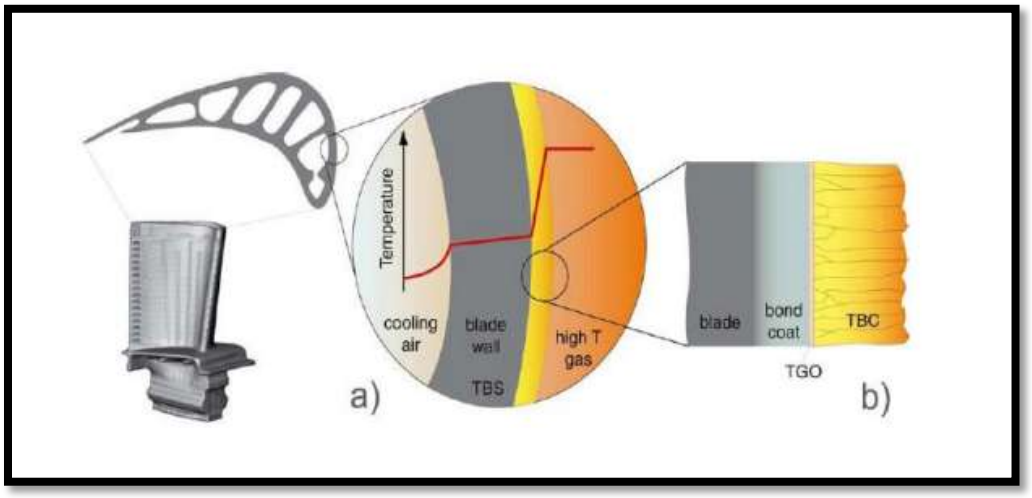

Figure 1: Schematic of a turbine engine blade. a.) zoomed in view showing the thermal gradient as a red line with the most change over the thermal barrier coating fallowed by the inside air cooling chambers. b.) zoomed in view showing the layers protecting the outer surface of the engine blade; bondcoat, thermally grown oxide(TGO) and thermal barrier coating (TBC).

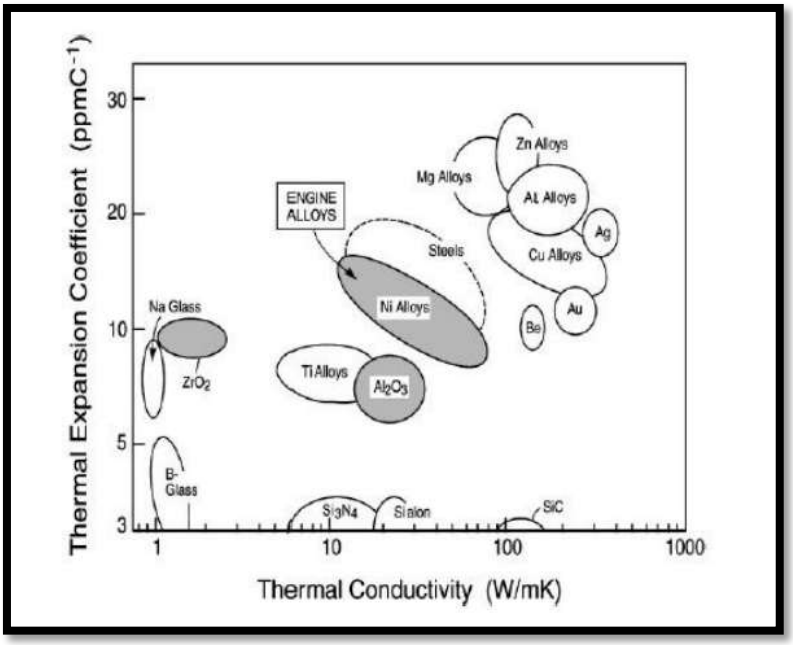

Figure 2: Compares thermal expansion coefficient and thermal conductivity for varying materials. Zirconia oxide and nickel alloys have similar thermal expansion coefficient, and zirconia oxide has a low thermal conductivity.

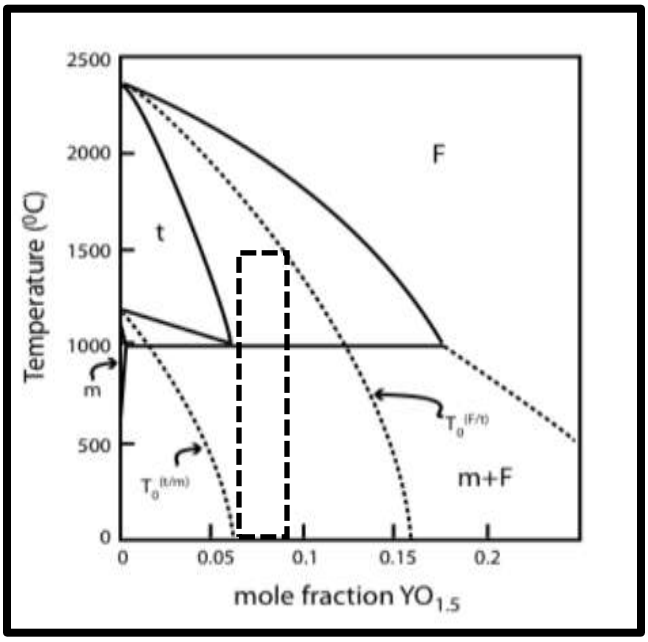

Figure 3: Phase diagram for low mole fractions of YO1.5-ZrO2, dashed box region is 7-8% yttria stabilized zirconia.

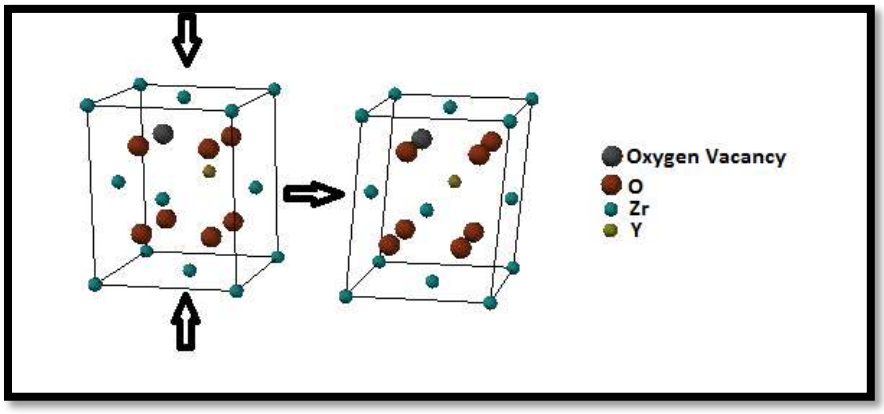

Figure 4: Schematic showing tetragonal to monoclinic transformation upon mechanical loading.

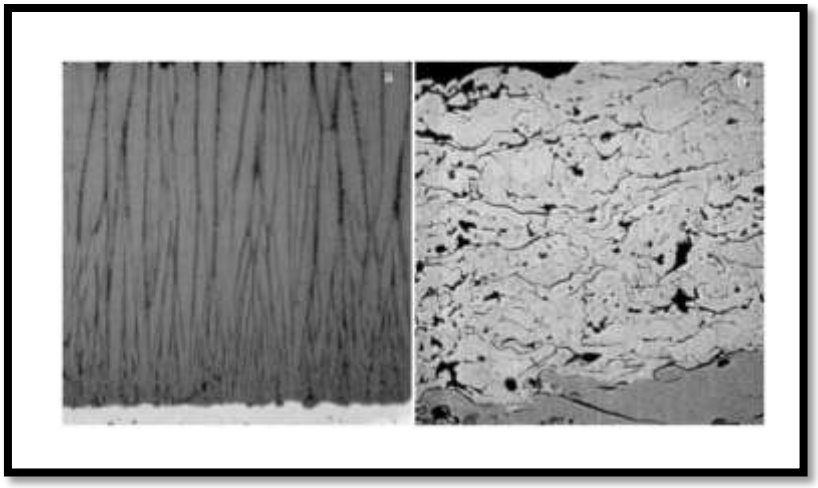

Figure 5: Two microstructures produced a.) Electron beam physical vapor deposition (EB-PVD) with columnar structure, b.) Air plasma sprayed (APS) resulting in a splat microstructure, when applying the top oxide coat of the thermal barrier coating.

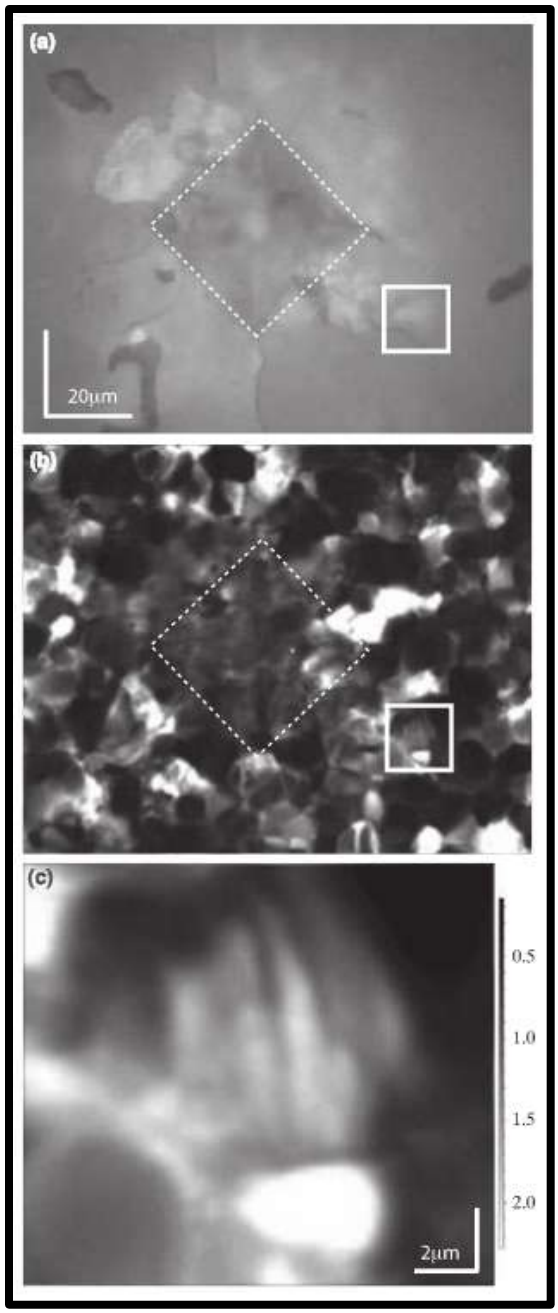

Figure 6: White-light and Raman images of indented region in the bulk material. Image (a) shows an image of the indent with radial crack emanating from the corners of the indent. The dashed box highlights the edges of the diamond indent whereas the solid box marks the region where high-resolution images were taken and are seen in section c of this image. Image (b) is a Raman map of the relative intensities of the B1g/A1g modes for the same region as seen in figure (a). Bright regions indicate that the c-axis is oriented out of the plane of the paper whereas dark regions indicate that it is within the plane. The presence of ferroelastic switching in the process zones can be observed by bright areas along the length of the cracks as well as the presence of banding in grains near the indent and cracks. Image (c) is a higher resolution image of the region boxed in figures (a) and (b). This image clearly illustrates the switching along the crack (lower left-hand corner) and the presence of ferroelastic domain bands in the bulk of the grain (image center).

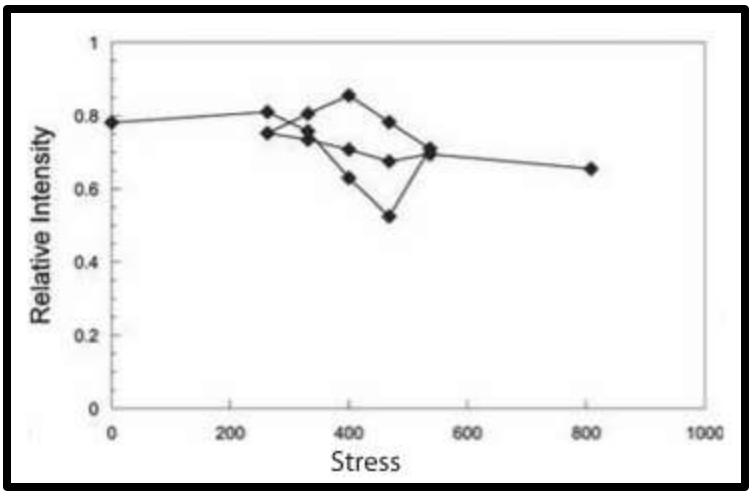

Figure 7: Figure showing the relative intensities of the B1g/A1g modes of 18 mol% ceria-stabilized zirconia as a function of uniaxial loading in the diamond anvil cell. Load measurements were taken using the luminescence of a ruby standard

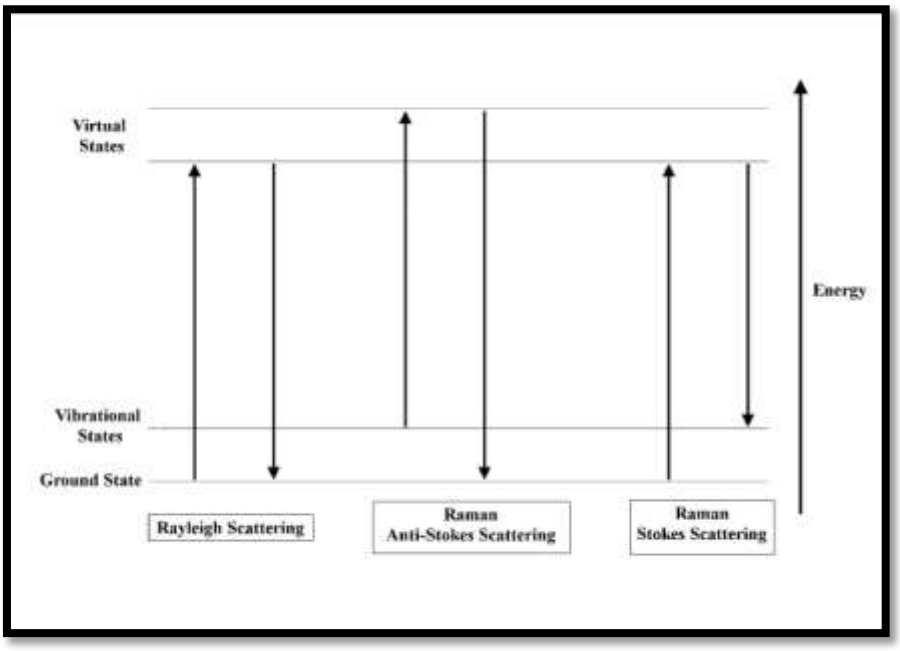

Figure 8: Photon scattering schematic: Rayleigh scattering is elastic scattering phenomenon where no energy is loss or gained to the photon. Stokes and Anti-Stokes are inelastic scattering phenomenon. Anti-Stokes photon gains energy during interaction with a material. Stokes the photon loses energy during the interaction with the material.

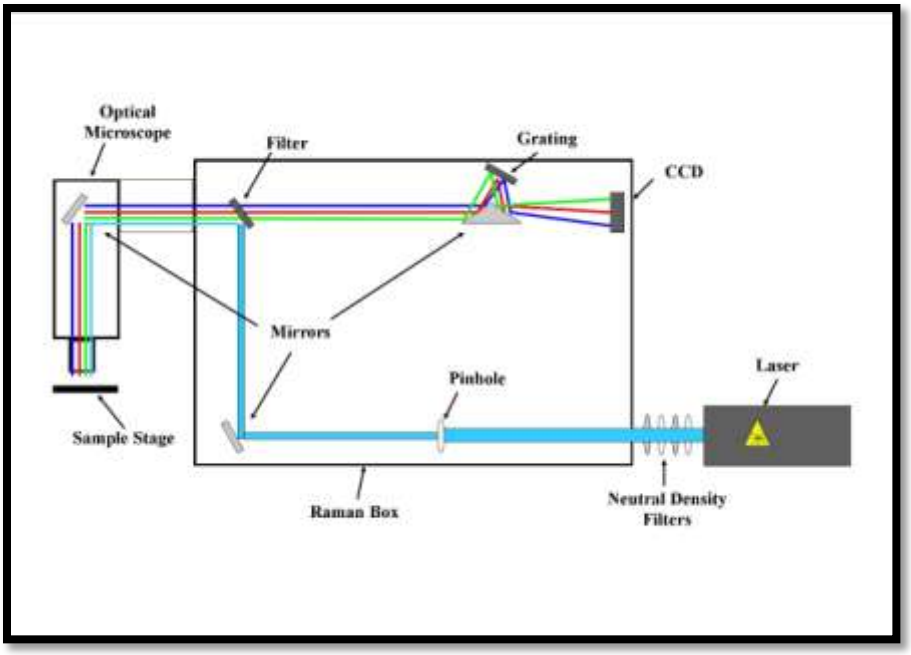

Figure 9: A simplifies schematic of the laser path inside a Raman spectrometer showing one wave frequency exist until interaction with the sample. Vibrational modes change the photons particles to a spectrum of frequencies which are deflected and collected at the charged couple-device (CCD) to analyze the material.

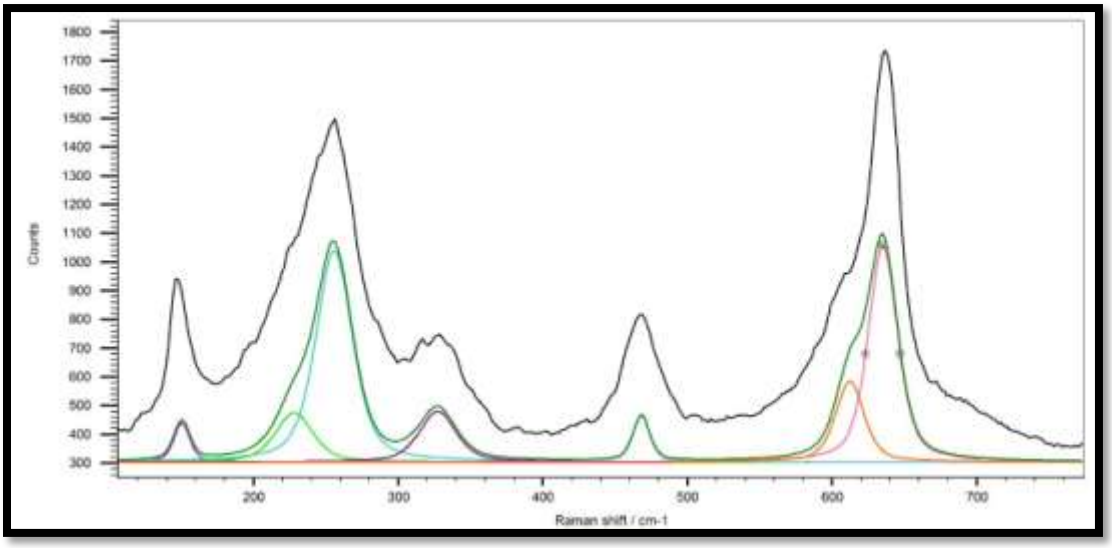

Figure 10: The top continuous line is a Raman spectra of tetragonal 8% YSZ. The bottom line is made from a series of peaks with varying intensities at different energies used to fit the 8% YSZ Raman spectrum. When the spectra are fit, the area, position, intensity and width of the peaks can be used to analyze the state, structure, and crystal orientation of material.

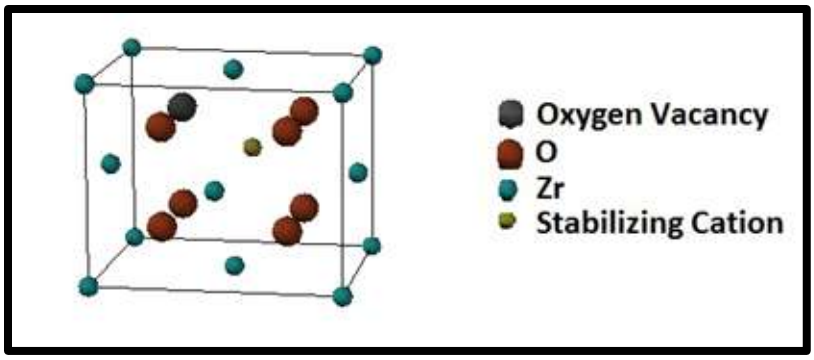

Figure 11: Schematic showing how zirconia is stabilized with tetrahedral coordinated cation. For every two cations added into the unit cell, one oxygen vacancy is created.

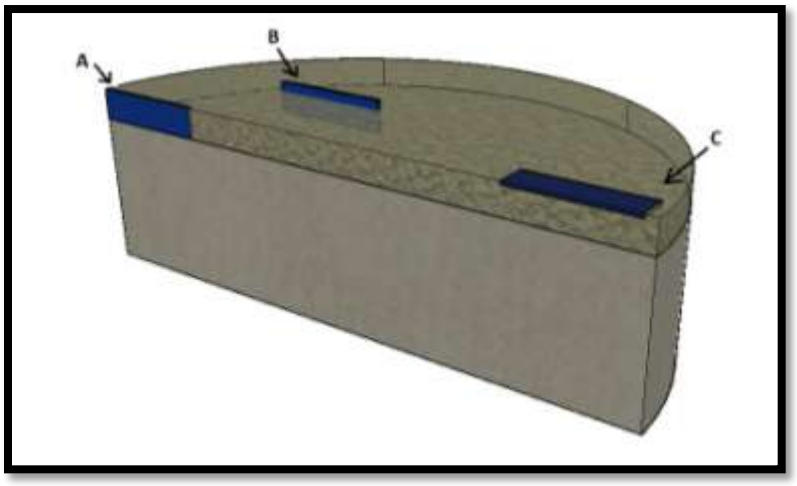

Figure 12: Three different positions on a sample where Raman maps were taken from. A.) The fracture surface where the side of the columns are analyzed from the top of the coating down to the substrate. B.) A Raman map from the top of the surface down to the substrate where the columns are not exposed. C.) A map off the top of the coating.

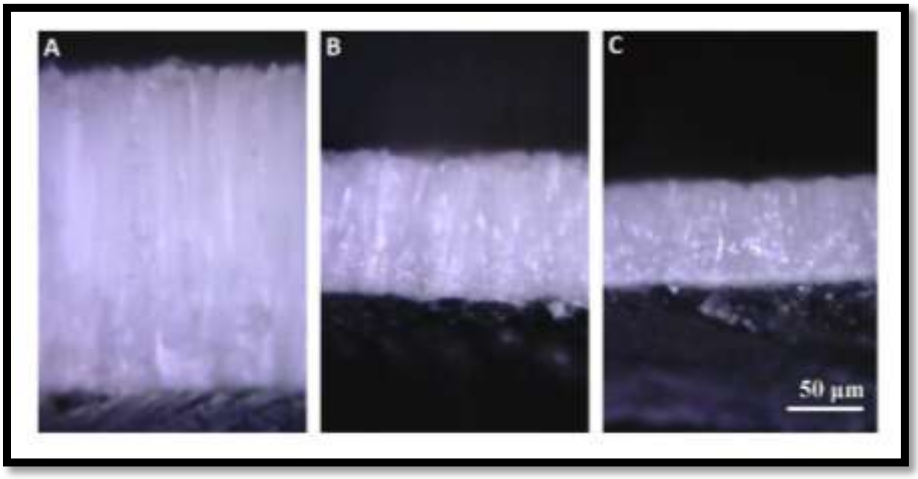

Figure 13: The thickness of the three coatings received from Canfield University. A.) as fabricated, B.) 30◦ impact angle from the surface, C.) 90◦ impact angle from the surface.

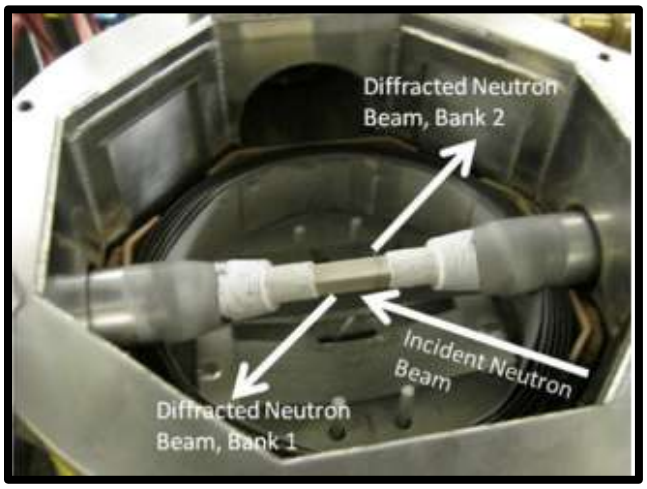

Figure 14: The high-temperature furnace on SMARTS setup. The detectors are located to the top right and the bottom left of the image. The neutron path into the sample is denoted with arrow.

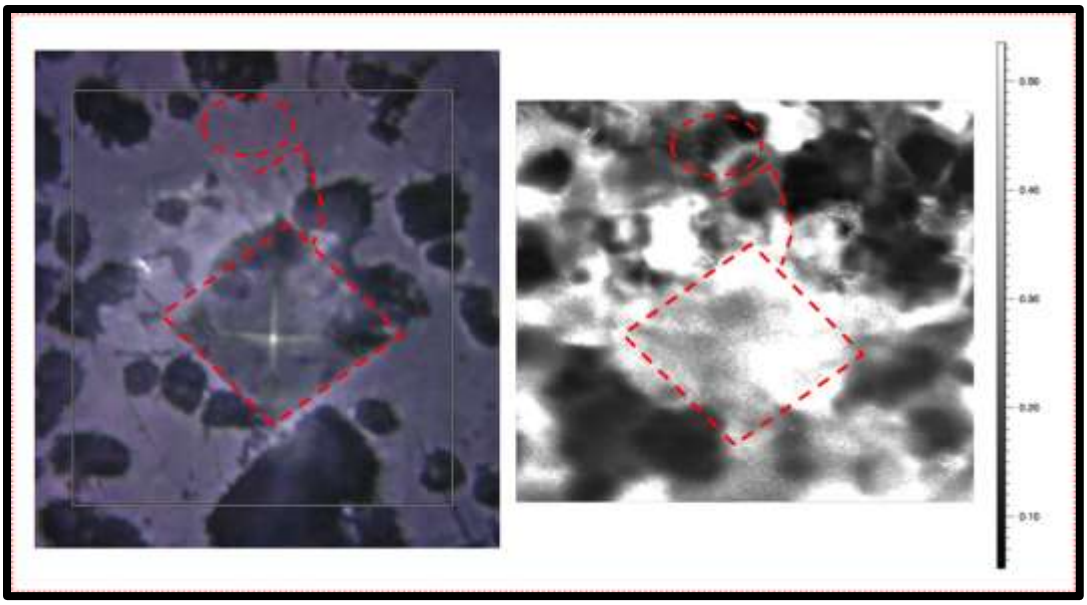

Figure 15: White light and Raman images of the B1g/A1g modes over an indention on 15CSZ. The dashed diamond outlines the indent on the surface, and the dashed lines represent a crack radiating from the top side of the indent. The dashed circle highlights a ferroelastic region where the bright regions indicate the c-axis out of plane.

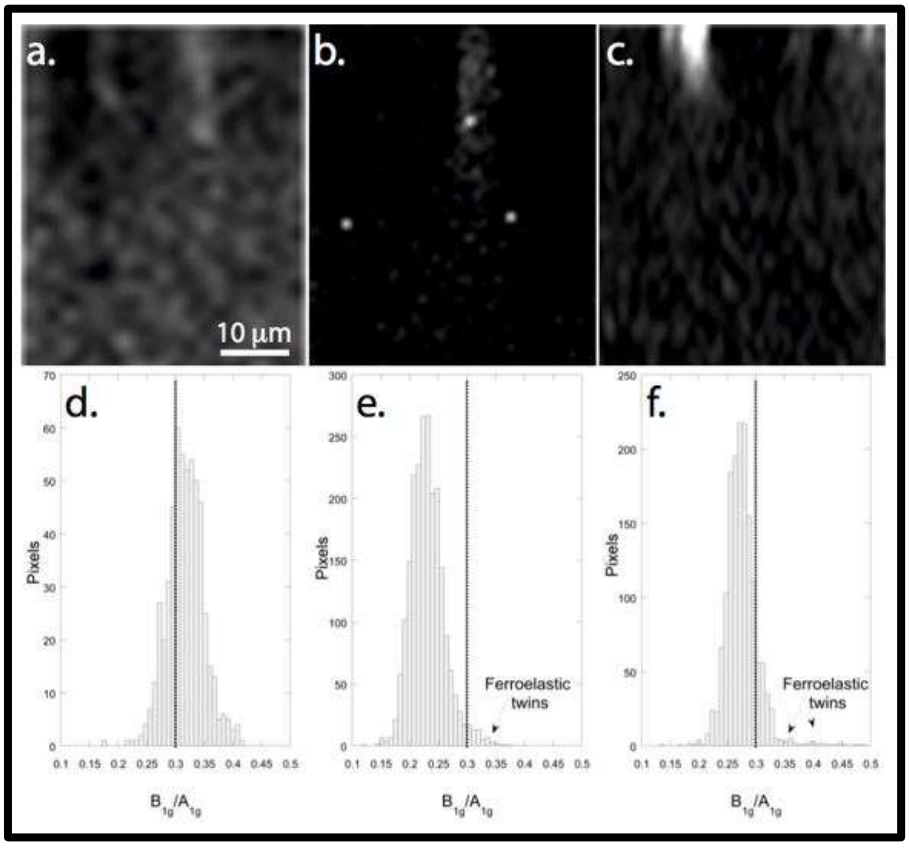

Figure 16: Raman "virtual cross section" images of a) as-deposited, b) 30° eroded, and c) 90° eroded EB-PVD coatings. These images were taken using the ratio of the areas of the B_{1g}/A_{1g} Raman modes. Histograms of the corresponding data in d, e, and f reveal both a plastic shearing of the eroded samples as well as the presence of ferroelastic twins in those samples.

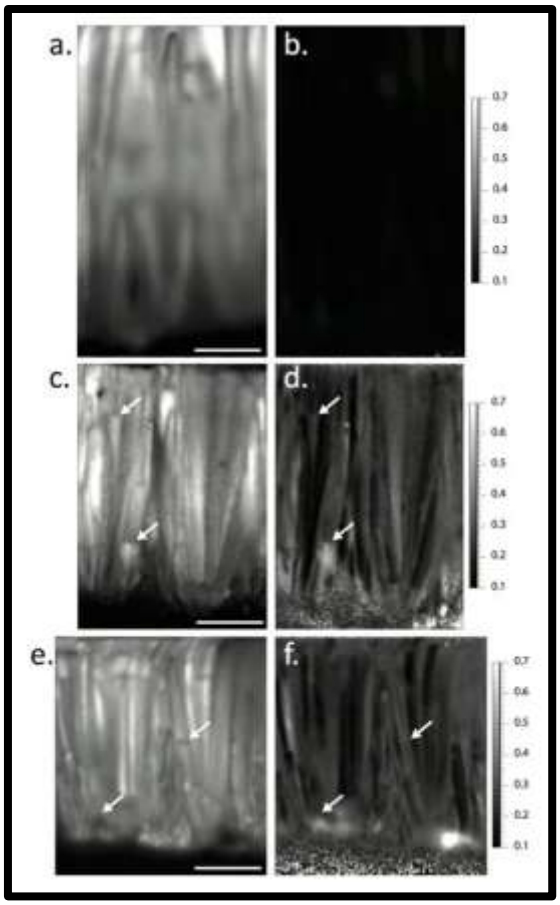

Figure 17: White light images for the a) as-deposited, c) 30° eroded, and e) 90° eroded EB-PVD coatings and the corresponding B_{1g}/A_{1g} ratio maps (b) as-deposited, d) 30° eroded, and f) 90° eroded). Images reveal no orientation changes in the as deposited coating and evidence of ferroelasticity in the eroded coatings. Arrows denote the locations of several cracks in the coatings.

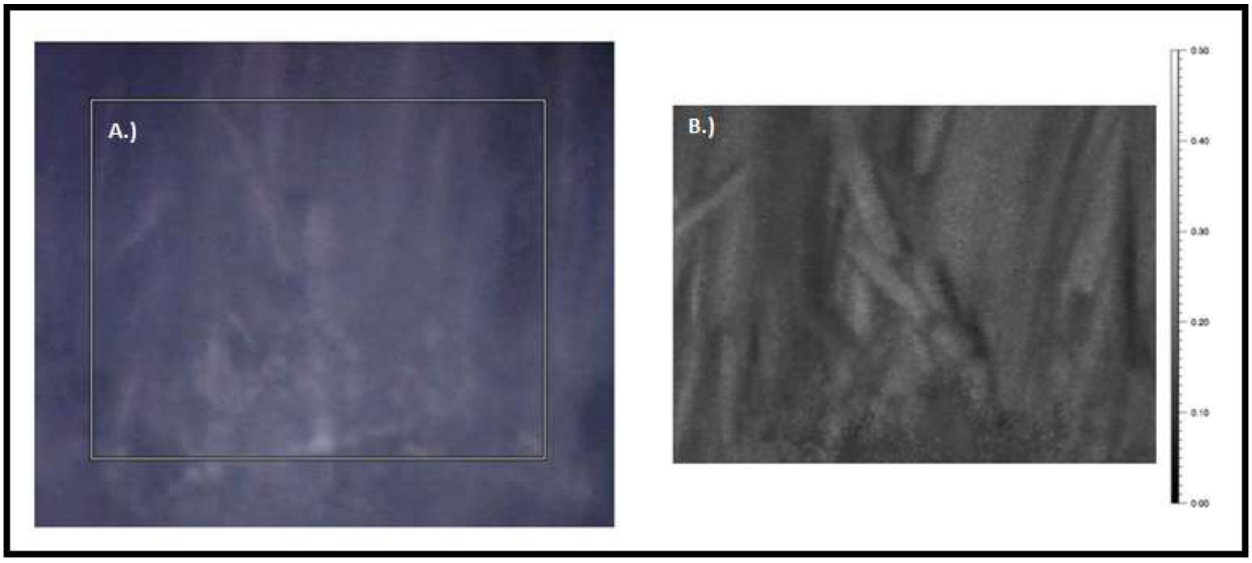

Figure 18: A.) White light image and B.) Raman images of the B1g/A1g modes over an indention on the side of as-deposited coating. The lighter regions are broken columns where the c-axis is pointing out of plane indicating ferroelastic switching along entire columns.

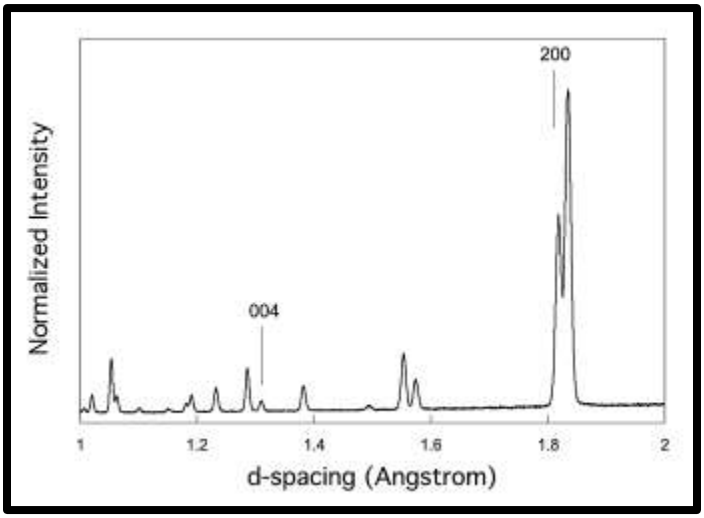

Figure 19: Neutron diffraction pattern for 18 mol% ceria doped zirconia at room temperature and no load. The {0 0 4} and {2 0 0} peaks are identified as the peaks used for determining the reorientation of the c-axis as a result of ferroelastic switching

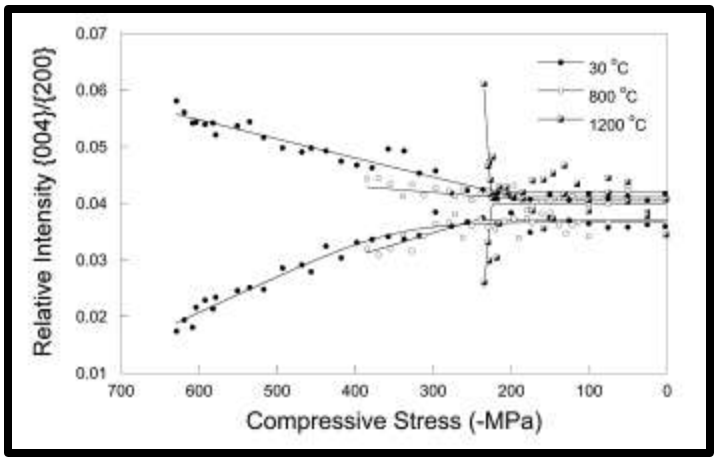

Figure 20: The relative intensities of the {0 0 4} peak divide by the {2 0 0}. The line on top for each of the sets above represents data taken from a collection bank perpendicular to the direction of load while the bottom represents a bank parallel to the direction of loading. The point at which the two lines for each set begin to diverge is identified as the coercive stress for the material. In this case coercive stress was measured to be approximate 250 MPa for all temperatures.

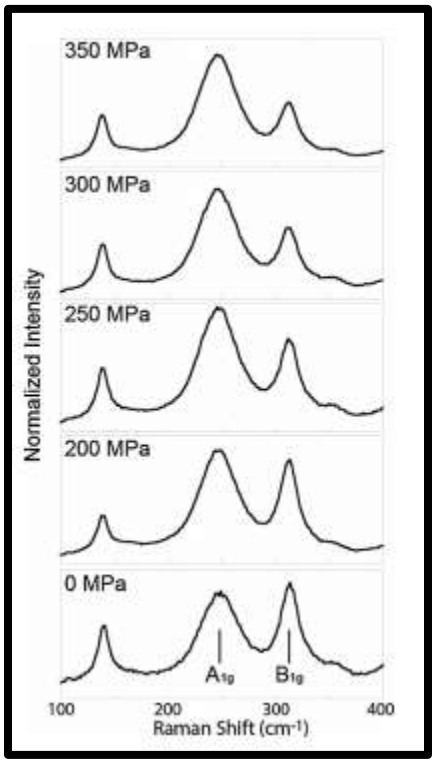

Figure 21: Raman spectra taken parallel to the loading direction as a function of load are seen above. The B1g mode, which is an indication of the c-axis being parallel to the laser excitation, and in this case parallel to the direction of loading, decreases in intensity as a function of load. These measurements were used to determine the coercive stress of the ceramic being tested.

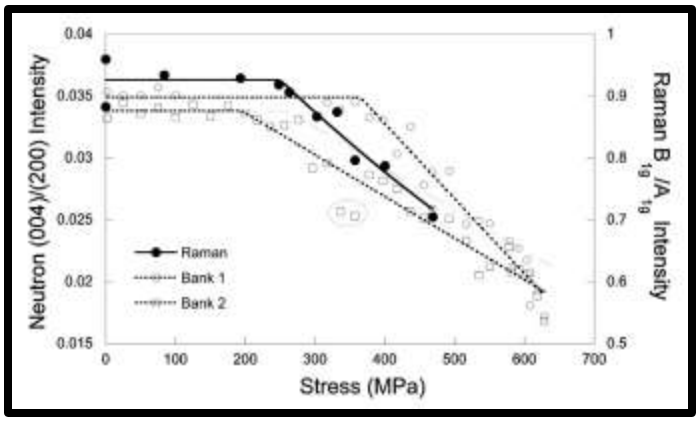

Figure 22: Ratio of the intensities of the out of plane orientation with respect to the in-plane orientation for both neutron and Raman data collected from both banks 1 and 2 at 30 ◦C. Both of the above techniques exhibit a deviation from linearity in the range of 250 MPa, the coercive stress as determined by the curve fits (dashed lines) using Eq. (2). The dot-dash line shows an alternate fitting of the data that does not include the circled data points.

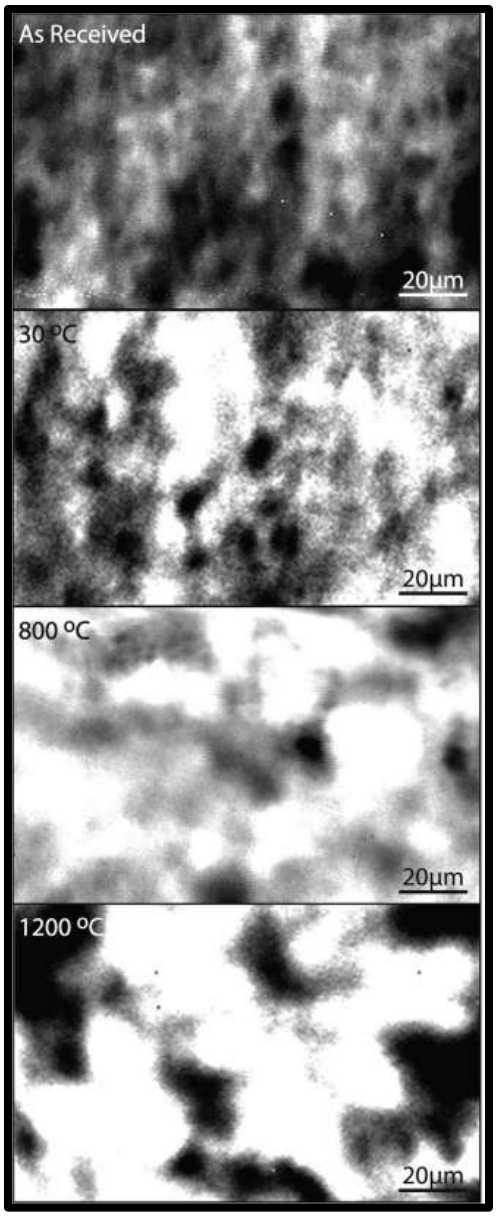

Figure 23: Raman orientation maps of the surfaces of samples tested in the SMARTS system at Los Alamos. Regions that appear bright have c-axis orientation pointed out of the plane of the page suggesting reorientation due to ferroelastic switching

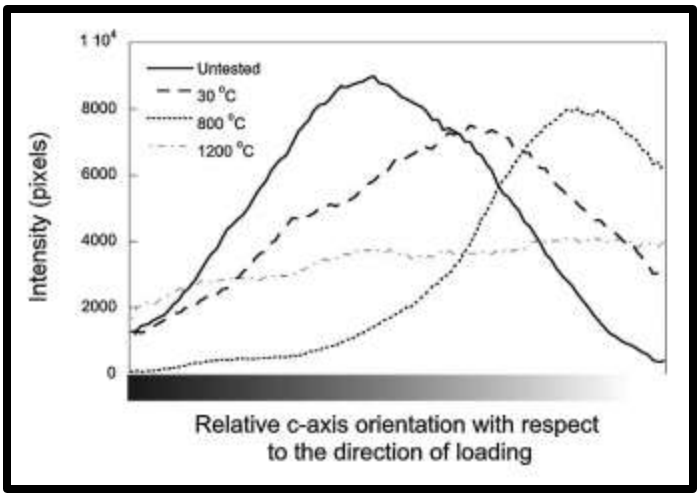

Figure 24: Histograms of the relative orientation of grains at the surface of samples loaded at temperature as measured by confocal Raman spectroscopy. The 1200 ◦C exclusively was polished lightly before this measurement to remove a thin layer of the monoclinic phase that had formed during testing.

Tables

Composition	liquid stabilizer (g)	zirconium acetate solution(g)
7 %YbSZ	8.19	41.06
7%ErSZ	5.32	41.19
7%NdSZ	5.43	41.71
7%LaSZ	5.37	41.84
7%GdSZ	6.21	41.41
12%CeSZ	13.02	38.64
15%CeSZ	16.09	36.9

Table 1: Grams of solution for reverse co-precipitation for 10 grams of 7 weight percent or rare earth oxide doped zirconia and 12 and 15 weight percent of cerium stabilized zirconia.

	As-Received	30^{o} Impact	90^{o} Impact
B_{1g}/A_{1g} Ratio	0.29	0.36	0.49
Standard Deviation	0.01	0.03	0.01

Table 2: B_{1g}/A_{1g} ratios for the As-Received, 30° impact, and 90° impact samples. Shows approximately a 40% increase in the B_{1g}/A_{1g} ratio for the 90° eroded sample with respect to the As-Received sample.

Referrences

[1]R.A. Miller, "Current status of thermal barrier coatings - an overview," *Surface & Coatings Technology,* **30**[1] 1-11 (1987).

[2]D.R. Clarke and C.G. Levi, "Materials design for the next generation thermal barrier coatings," *Annual Review of Materials Research,* **33** 383-417 (2003).

[3]S.M. Meier and D.K. Gupta, "The evolution of thermal barrier coatings in gas-turbine engine applications," *Journal of Engineering for Gas Turbines and Power-Transactions of the Asme,* **116**[1] 250-257 (1994).

[4]M.J. Stiger, N.M. Yanar, M.G. Topping, F.S. Pettit, andG.H. Meier, "Thermal barrier coatings for the 21st century," *Zeitschrift Fur Metallkunde,* **90**[12] 1069-1078 (1999).

[5]A.G. Evans, D.R. Clarke, andC.G. Levi, "The influence of oxides on the performance of advanced gas turbines," *Journal of the European Ceramic Society,* **28**[7] 1405-1419 (2008).

[6]N.P. Padture, M. Gell, andE.H. Jordan, "Materials science-thermal barrier coatings for gas-turbine engine applications," *Science,* **296**[5566] 280-284 (2002).

[7]D.M. Zhu and R.A. Miller, "Sintering and creep behavior of plasma-sprayed zirconia- and hafnia-based thermal barrier coatings," *Surface & Coatings Technology,* **108**[1-3] 114-120 (1998).

[8]V. Lughi, V.K. Tolpygo, andD.R. Clarke, "Microstructural aspects of the sintering of thermal barrier coatings," *Mater. Sci. Eng. A-Struct. Mater. Prop. Microstruct. Process.,* **368**[1-2] 212-221 (2004).

[9]R.G. Wellman and J.R. Nicholls, "A review of the erosion of thermal barrier coatings," *J. Phys. D-Appl. Phys.,* **40**[16] R293-R305 (2007).

[10]J.R. Nicholls, R.G. Wellman, andM.J. Deakin, "Erosion of thermal barrier coatings," *Materials at High Temperatures,* **20**[2] 207-218 (2003).

[11]C.Q. Ru and R.C. Batra, "Toughening due to transformations induced by a crack-tip stress-field in ferroelastic materials," *Int. J. Solids Struct.,* **32**[22] 3289-3305 (1995).

[12]C. Mercer, J.R. Williams, D.R. Clarke, andA.G. Evans, "On a ferroelastic mechanism governing the toughness of metastable tetragonal-prime (t ') yttria-stabilized zirconia," *Proc. R. Soc. A-Math. Phys. Eng. Sci.,* **463**[2081] 1393-1408 (2007).

[13]A.V. Virkar and R.L.K. Matsumoto, "Ferroelastic domain switching as a toughening mechanism in tetragonal zirconia," *Journal of the American Ceramic Society,* **69**[10] C224-C226 (1986).

[14]D. Porter, A.G. Evans, andA.H. Heuer, "Transformation-toughening in partially-stabilized zircocnia (psz)," *Acta Metallurgica,* **27** 1649-1654 (1979).

[15]D. Green, R.H.J. Hannink, andM. Swain, "Transformation toughening of ceramics." CRC Press: Boca Raton, FL, (1989).

[16]D. Marshall, "Strength characteristics of transformation-toughened zirocnia," *J. Am. Ceram. Soc.,* **69**[3] 173-180 (1986).

[17]P. Kelly and L. Rose, "The martensitic transformation inceramics--its role in transformation toughening," *Prog. Mater. Sci.,* **47**[5] 463-557 (2002).

[18]V. Sergo, V. Lughi, G. Pezzotti, E. Lucchini, S. Meriani, N. Muraki, G. Katagiri, S. Lo Casto, andT. Nishida, "The effect of wear on the tetragonal-to-monoclinic transformation and the residual stress distribution in zirconia-toughened alumina cutting tools," *Wear,* **214**[2] 264-270 (1998).

[19]J.W. Hutchinson and A.G. Evans, "On the delamination of thermal barrier coatings in a thermal gradient," *Surface & Coatings Technology,* **149**[2-3] 179-184 (2002).
[20]H.B. Zhao, Z. Yu, andH.N.G. Wadley, "The influence of coating compliance on the delamination of thermal barrier coatings," *Surface & Coatings Technology,* **204**[15] 2432-2441 (2010).
[21]N. Rebollo, A. Gandhi, andC.G. Levi, "Phase sbatility issues in emerging tbc systems," pp. 431-442. in High temperature corrosion and materials chemistry iv, **Vol. 2003.** Electrochemical Society Series, 2003.
[22]C.G. Levi, "Emerging materials and processes for thermal barrier systems," *Current Opinion in Solid State & Materials Science,* **8**[1] 77-91 (2004).
[23]S. Stecura, "86905 optimization of the nicral-y/zro2-y2o3 thermal barrier system." in NASA Technical Bulletin**.** NASA, 1985.
[24]S. Stecura, "78976 effect of compositional changes on the performance of thermal barrier coatings systesm." in NASA Technical Memorandum**.** NASA, Lewis Research Center Cleveland, OH 44135, 1979.
[25]W. Beele, G. Marijnissen, andA. Van Lieshout, "The evolution of thermal barrier coatings - status and upcoming solutions for today's key issues," *Surface & Coatings Technology,* **120** 61-67 (1999).
[26]R. Mcpherson, "A review of microstructure and properties of plasma sprayed ceramic coatings," *Surface & Coatings Technology,* **39**[1-3] 173-181 (1989).
[27]H.B. Zhao, C.G. Levi, andH.N.G. Wadley, "Vapor deposited samarium zirconate thermal barrier coatings," *Surface & Coatings Technology,* **203**[20-21] 3157-3167 (2009).
[28]U. Schulz and M. Schmucker, "Microstructure of zro2 thermal barrier coatings applied by eb-pvd," *Materials Science and Engineering A,* **276**[1-2] 1-8 (2000).
[29]R.G. Wellman and J.R. Nicholls, "Some observations on erosion mechanisms of eb pvd tbcs," *Wear,* **242**[1-2] 89-96 (2000).
[30]R.G. Wellman and J. Nicholls, "A mechanism for the erosion of eb pvd tbcs," pp. 531-538. in High temperature corrosion and protection of materials 5, pts 1 and 2, **Vol. 369-3.** *Materials science forum.* Edited by R. Streiff, I.G. Wright, R.C. Krutenat, M. Caillet, andA. Galerie, 2001.
[31]A.G. Evans, "Perspective on the development of high-toughness ceramics," *Journal of the American Ceramic Society,* **73**[2] 187-206 (1990).
[32]T. Marrow, S. Roberts, andA. Pearce-Higgins, "The brittle/ductile transition in cubic stabilized zirconia," *Journal of the European Ceramic Society,* **14** 447-453 (1994).
[33]D. Porter and A.H. Heuer, "Mechanisms of toughening partially bstabilized zirconia (psz)," *Journal of the American Ceramic Society,* **60**[3-4] 183-184 (1977).
[34]D. Porter and A.H. Heuer, "Microstructral development in mgo-partially stabilized zirconia (mg-psz)," *Journal of the American Ceramic Society,* **62**[5-6] 298-305 (1979).
[35]A.H. Heuer, N. Claussen, W. Kriven, andM. Ruhle, "Stability of tetragonal zro2 particles in ceramic matrices," *Journal of the American Ceramic Society,* **65**[12] 642-650 (1982).
[36]A.H. Heuer and M. Ruhle, "Phase transformations in zro2-containg ceramics: I, the instability of c-zro2 and the resulting diffusion controlled reactions." in Advances in ceramics, **Vol. 12, Science and Technology of Zirconia II.** Edited by N. Claussen, M. Ruhle, andA.H. Heuer. American Ceramic Society, Columbus, OH, 1984.
[37]T. Tsukuma, Y. Kubota, andT. Tsukidate, "Thermal and mechanical properties of y2o3-stabilized zirconia polycrystal," pp. 382-390. in Advances in ceramics, **Vol. 12, Science**

and Technology of Zirconia II. Edited by N. Claussen, M. Ruhle, andA.H. Heuer. America Ceramic Society, Coloumbus, OH, 1984.
[38]D. Michel, L. Mazerolles, andM. Perez Y Jorba, "Fracture of metastable tetragonal zirconia single crystals," *Journal of Materials Science,* **18** 2618-2628 (1983).
[39]F.M. Pitek and C.G. Levi, "Opportunities for tbcs in the zro2-yo1.5-tao2.5 system," *Surface & Coatings Technology,* **201**[12] 6044-6050 (2007).
[40]T.A. Schaedler, R.M. Leckie, S. Kramer, A.G. Evans, andC.G. Levi, "Toughening of nontransformable t '-ysz by addition of titania," *Journal of the American Ceramic Society,* **90**[12] 3896-3901 (2007).
[41]T.A. Schaedler, "Unpublished work." in**.** GE Aviation, 2008.
[42]E. Smith and G. Dent, "Modern raman spectroscopy--a practical approach.″ John Wiley & Sons, Ltd: West Sussex, England, (2005).
[43]A. Loganathan and A. Gandhi, "Fracture toughness of t' zro2 stabilised with mo1.5 (m=y,yb & gd) for thermal barrier applications," *Transactions fo the Indian Institute of Metals,* **64**[1-2] 71-74 (2011).
[44]P. Duwez and F. Odell, "Phase relationships in the system zirconia-ceria," *Journal of the American Ceramic Society,* **33**[9] 274-283 (1950).
[45]A. Bolon, T. Sisneros, A. Schubert, B. Bclausen, D. Brown, andM. Gentleman, "Comparison of neutron diffraction and raman spectroscopic studies of the ferroelastic behavior of ceria-stabilized zirconia at elevated temperatures," *Journal of the European Ceramic Society,* **35**[2] 623-629 (2014).
[44]A. Bolon and M. Gentleman, "Raman spectroscopic observations of ferroelastic switching in ceria stabilized zirconia " *J. Am. Ceram. Soc.,* **94**[12] 4478-4482 (2011).
[45]A. Bolon, T. Sisneros, A. Schubert, B. Bclausen, D. Brown, andM. Gentleman, "Comparison of neutron diffraction and raman spectroscopic studies of the ferroelastic behavior of ceria-stabilized zirconia at elevated temperatures," *Journal of the European Ceramic Society,* **35**[2] 623-629 (2014).